Catalysis Science & Technology

PAPER

View Article Online
View Journal | View Issue

Cite this: *Catal. Sci. Technol.*, 2019, **9**, 2211

Redox oxidative cracking of *n*-hexane with Fe-substituted barium hexaaluminates as redox catalysts†

Xin Tian,[ab] Ryan B. Dudek,[a] Yunfei Gao,[a] Haibo Zhao*[b] and Fanxing Li *[a]

Light olefins such as ethylene and propylene are critical building blocks in the chemical industry and are currently produced mainly from steam cracking of naphtha. However, the highly endothermic nature of steam generation and the cracking reactions make this process highly energy- and CO_2-intensive. Coke formation in the steam cracker tubes represents another obstacle. To address these challenges, we proposed a chemical looping approach to convert naphtha into olefins *via* a redox oxidative cracking (ROC) process. In the present work, Fe-substituted barium hexaaluminates ($BaFe_xAl_{12-x}O_{19}$) were investigated as oxygen carriers, or redox catalysts, to convert *n*-hexane to olefins *via* ROC. The cyclic redox scheme facilitated by the Fe-substituted hexaaluminates allows autothermal operation and higher olefin yields relative to the endothermic steam-cracking process. While base $BaFe_xAl_{12-x}O_{19}$ (x = 1, 2, 3, 4, 6) oxides showed high CO_x yields (8.4–55.2%) in ROC of *n*-hexane, 20 wt% Na_2WO_4 promotion of $BaFe_6Al_6O_{19}$ (20-NaW/BaFe6) significantly inhibited CO_x formation (0.6–1.2% CO_x yield) while oxidizing all the H_2 produced during cracking within a temperature range of 600–700 °C and GHSV of 9000 h^{-1}. Benefiting from the donation of selective lattice oxygen, 20-NaW/BaFe6 more than doubled the olefin yield when compared to that from thermal cracking (26.0% *vs.* 12.8%). Moreover, decreasing the GHSV from 9000 h^{-1} to 2250 h^{-1} resulted in 8.5% increase in *n*-hexane conversion on an absolute basis, while maintaining nearly the same olefin selectivity. Long-term stability of the 20-NaW/BaFe6 oxygen carrier was also demonstrated within 30 cycles at 700 °C and 2250 h^{-1}, achieving an olefin yield in the range of 31.3–32.4% and low CO_x yield of 0.6–0.7%. XPS analysis of cycled BaFe6 revealed a shift towards near-surface Ba enrichment upon redox cycling. In comparison, both as-prepared and cycled 20-NaW/BaFe6 showed suppression of near surface Ba content, indicating that Na_2WO_4 inhibited the migration of Ba into the near-surface region during *n*-hexane ROC and effectively suppressed non-selective oxidation reactions.

Received 18th December 2018,
Accepted 1st April 2019

DOI: 10.1039/c8cy02530d

rsc.li/catalysis

Introduction

Ethylene is a key organic material in the chemical industry due to its extensive application as a building block for the production of acetaldehyde, ethylbenzene, ethylene glycol, polyethylene, and many other derivatives.[1,2] To date, ethylene is principally produced by steam cracking of hydrocarbon feedstocks such as naphtha, ethane, and gas oil.[3,4] In 2016, the worldwide market demand for ethylene was over 160 million tons, mostly produced from thermal cracking of naphtha (42.6%) and ethane (36.3%).[5]

In a typical naphtha cracking process, liquid-phase naphtha is first preheated, vaporized, and diluted with steam in a convection furnace. The gaseous mixture is then introduced into a radiant tube reactor (750–900 °C) and cracked into light hydrocarbons and H_2 *via* complex gas-phase reactions.[6] Although steam cracking of naphtha is a well-established commercial process, challenges are still present in its high energy consumption and CO_2 emissions. Due to the highly endothermic nature and the complex downstream product separation process, steam cracking was ranked as one of the most energy-intensive processes in the chemical industry.[7,8] For instance, 1 ton of ethylene production from naphtha steam cracking would require approximately 28.5 GJ of thermal energy input and lead to 1.9 tons of CO_2 emissions.[7] Coke deposition is an accompanying issue in steam cracking, which requires frequent cracking reactor shutdown for coke removal.[9] With the continuing growth in ethylene market demand into

[a] *Department of Chemical & Biomolecular Engineering, North Carolina State University, Raleigh, NC 27695, USA. E-mail: fli5@ncsu.edu*
[b] *State Key Laboratory of Coal Combustion, School of Energy and Power Engineering, Huazhong University of Science and Technology, Wuhan 430074, PR China. E-mail: hzhao@mail.hust.edu.cn*

† Electronic supplementary information (ESI) available. See DOI: 10.1039/c8cy02530d

the foreseeable future, novel techniques for more sustainable and energy-efficient ethylene production from naphtha are highly desirable.

Catalytic cracking of naphtha with heterogeneous catalysts such as zeolites,[10–14] which lowers the cracking temperature, represents an alternative to steam cracking. Nevertheless, significant thermal energy input for naphtha vaporization and cracking is still required.[15,16] To address the endothermicity issue, oxidative cracking of naphtha with O_2 co-feed has been proposed.[17] Under this scheme, the heat requirement of the endothermic cracking process can be met by the combustion of H_2 (and other hydrocarbons *via* non-selective combustion) with gaseous O_2. Liu *et al.* compared the production of light alkenes by gas phase oxidative cracking (GOC) and catalytic oxidative cracking (COC) of *n*-hexane.[18,19] For the non-catalytic GOC of *n*-hexane,[18] the *n*-hexane conversion reached 85% at 750 °C, with 50% yield of light alkenes. For the COC of *n*-hexane over three different catalysts,[19] *i.e.*, HZSM-5, 10% La_2O_3/HZSM-5, and 0.25% Li/MgO, the best cracking performance was achieved by the 0.25% Li/MgO, with 64% *n*-hexane conversion and 67% olefin selectivity at 700 °C. However, in both GOC and COC processes, significant CO_x compounds (14.2–15.4% CO_x selectivity) were produced from non-selective combustion reactions. Boyadjian *et al.* further tested the Li/MgO catalyst for COC of *n*-hexane at lower temperatures, achieving 16.8% olefin yield from 28.4% *n*-hexane conversion at 575 °C. However, CO_x selectivity was still high (24.6%) and the relatively low O_2 conversion (65.2%) can create complications in downstream gas separations.[20] Additionally, the coexistence of gaseous O_2 and hydrocarbons in the COC and GOC crackers introduces safety hazards and requires the use of energy-intensive air separation units to produce gaseous O_2.

Using lattice oxygen supplied by an oxygen carrier (also known as a redox catalyst), chemical looping offers an alternative strategy for oxidative naphtha cracking without the issues associated with O_2 co-feed.[21] In this redox oxidative cracking (ROC) process, naphtha cracking is completed in two spatially separate reactors, as shown schematically in Fig. 1. In the oxidative cracking reactor, light olefins and H_2 are produced from naphtha cracking, with H_2 being selectively combusted by the lattice oxygen donated from the redox catalyst. The reduced catalyst material subsequently recuperates oxygen from air in a separate regeneration reactor to complete the redox loop. The ROC process is potentially advantageous compared to traditional steam cracking and GOC/COC processes in three aspects: 1) avoiding direct contact between O_2 (air) and naphtha mitigates safety concerns and avoids costly air separation unit by using lattice oxygen instead of gaseous O_2; 2) the use of lattice oxygen instead of O_2 potentially inhibits non-selective combustion of light olefin products; 3) the elimination of air separation units and *in situ* combustion of H_2 facilitates improved energy conversion efficiency.[21]

Despite the various potential advantages possessed by the ROC scheme, studies on ROC of naphtha are relatively few to date. Elbadawi *et al.* investigated the oxidative cracking of *n*-hexane under a cyclic redox scheme, using VO_x/Ce–Al_2O_3 as oxygen carrier.[22] For reaction tests conducted within the temperature range of 525–600 °C, the highest *n*-hexane conversion of 33% was attained at 600 °C. However, CO_x selectivity was as high as 27.3% on a carbon basis. Additionally, significant CH_4 was co-produced during the reaction (~30% CH_4 selectivity). The high selectivity towards low-value methane and CO_x weakened the merits of naphtha ROC, illustrating the critical importance of selecting a suitable redox catalyst with the desired activity and selectivity. Moreover, physical and chemical stability is another critical requirement for the oxygen carrier in the cyclic redox mode.[23]

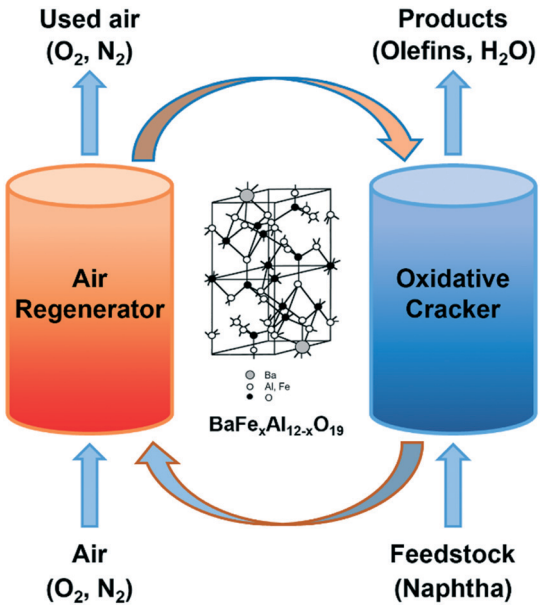

Fig. 1 A schematic view of redox oxidative cracking (ROC) of naphtha using $BaFe_xAl_{12-x}O_{19}$ as redox catalysts.

Barium hexaaluminate ($BaAl_{12}O_{19}$, BHA), with layered structures consisting of alternating γ-Al_2O_3 spinel blocks and mirror planes, has been extensively studied in catalytic CH_4 combustion and high-temperature N_2O decomposition processes.[24–26] Recently, transition metal-substituted hexaaluminates were found to exhibit promising reactivity and high sintering resistance in chemical looping combustion and reforming processes.[27,28] Fe-substituted BHAs have been investigated as oxygen carriers in chemical looping combustion (CLC) of CH_4. $BaFe_3Al_9O_{19}$ achieved high reactivity (80% CH_4 conversion and 100% selectivity to CO_2) during 10 redox cycles at 800 °C. The stable redox activity was attributed to the preservation of the hexaaluminate structure during the reduction step with CH_4, which prevents the oxygen carrier particles from agglomerating in the subsequent regeneration step with air.[27] Given the fact that BHA has a stable structure and most of the Al sites can be substituted by Fe cations,[29] Fe-substituted BHAs are expected to have sufficient oxygen donating capacity and physical stability, potentially suitable for application as redox catalysts in ROC of naphtha.

In the current study, we investigated the performance of a series of Fe-substituted BHAs ($BaFe_xAl_{12-x}O_{19}$, with different

levels of Fe substitution) for naphtha ROC. We note that naphtha is a complex mixture and would be challenging to study from both reaction and mechanistic standpoints. As such, the present study focuses on the study of *n*-hexane, which is a frequently used model compound of naphtha. Comparisons were made between base $BaFe_xAl_{12-x}O_{19}$ samples and sodium tungstate (Na_2WO_4) promoted $BaFe_xAl_{12-x}O_{19}$ samples, and the effect of Na_2WO_4 loading was studied. Promotion of the base sample with Na_2WO_4 was expected to alter the physical and chemical properties of the redox catalyst surface, thus tuning its selectivity towards different reaction products. Reactivity tests of these samples were conducted at various temperatures and gas hourly space velocities (GHSV). While base $BaFe_xAl_{12-x}O_{19}$ oxides showed relatively high CO_x selectivity in ROC of *n*-hexane, Na_2WO_4 promotion was found to be very effective to improve light olefins selectivity, albeit lowered *n*-hexane conversion when compared to their unpromoted counterparts. 20 wt% Na_2WO_4-promoted $BaFe_6Al_6O_{19}$ (hereafter, 20-NaW/BaFe6) showed significant increase in olefin yields compared to thermal cracking at all temperature conditions tested. Meanwhile, all of the H_2 produced was selectively combusted with relatively low CO_x selectivity at 600–700 °C and 9000 h^{-1}. XRD, BET and XPS characterizations were used to evaluate the redox catalysts before and after reaction testing, as well as to reveal the relationship between reaction performance and near-surface elemental compositions. Long-term cyclic redox tests were further conducted to verify the chemical and physical stability of 20-NaW/BaFe6 in the ROC scheme.

Experimental

Redox catalysts synthesis

The redox catalysts tested in the current study are variations on the barium hexaaluminate phase, in which Al^{3+} ions were substituted by Fe^{3+} to different extents, leading to a $BaFe_xAl_{12-x}O_{19}$ (x = 1, 2, 3, 4, 6) stoichiometry. They were prepared *via* the co-precipitation method similar to that described in literature.[29,30] Taking the preparation of 3 g of $BaFe_6Al_6O_{19}$ as an example, 0.84 g $Ba(NO_3)_2$ (99.0%, Sigma-Aldrich) and 7.75 g $Fe(NO_3)_2{\cdot}9H_2O$ (99.0%, Sigma-Aldrich) were first dissolved in deionized water at 60 °C to attain a clear solution. HNO_3 (99.0%, Sigma-Aldrich) was used to acidify the attained solution to pH ≈ 1, and 7.20 g $Al(NO_3)_3$ (99.0%, Sigma-Aldrich) was further dissolved. The mixed nitrate solution was then poured into a saturated $(NH_4)_2CO_3$ (99.0%, Sigma-Aldrich) solution at 300% excess under vigorous stirring. Hexaaluminate precursors were formed during the precipitation. After aging at 60 °C for 3 h under continuous stirring, the precipitates were filtered by vacuum filtration. The cake-like precipitates were repeatedly washed with deionized water and then dried overnight in oven at 110 °C. Finally, the dried precursors were first calcined at 450 °C for 3 h in a muffle furnace and then further sintered at 1300 °C for 6 h in a tube furnace (GSL-15 0X, MTI Corporation) in air flow. The high temperature sintering led to the formation of the desired hexaaluminate phase.

Further promotion of the as-prepared $BaFe_6Al_6O_{19}$ sample with Na_2WO_4 was conducted using the wet impregnation method with various amounts of Na_2WO_4 addition (5 wt%, 10 wt%, and 20 wt%). Calculated amount of $Na_2WO_4{\cdot}2H_2O$ (99.0%, Sigma-Aldrich) was dissolved in deionized water and the Na_2WO_4 solution was dropwise added to the base $BaFe_6Al_6O_{19}$ sample. After being magnetically stirred for 30 min, each sample was kept in an oven at 80 °C for 12 h. Finally, the Na_2WO_4-promoted $BaFe_6Al_6O_{19}$ samples were calcined at 900 °C for 6 h in a muffle furnace. All the samples were crushed and sieved, using particles in the size range of 250–850 μm for reaction tests, and powders smaller than 250 μm for characterization.

Characterization of redox catalysts

Several characterization techniques were used to study the crystalline phase, surface area, pore size distribution, and near-surface composition of the redox catalysts before and after redox cycling. Powder X-ray diffraction (XRD) was carried out to reveal the possible changes in crystal phase and crystallite size of the samples before and after reaction. A Rigaku SmartLab X-ray diffractometer with monochromatic Cu-Kα as radiation source (λ = 0.1542 nm) was used for the characterization, operating at 40 kV and 44 mA. Stepwise scan method with a 0.05° step size and holding time of 3 s was applied to attain XRD patterns, within a 2θ range of 10–80°. Crystal phase determination of the samples was realized by processing the XRD patterns in the HighScore Plus software, using the International Center for Diffraction Data (ICDD) database. BET surface area and pore size distribution of the samples were quantified by a Micromeritics ASAP 2020 accelerated surface area and porosity system, using multipoint N_2 physisorption method at 77.3 K. Prior to adsorption measurements, all samples were degassed overnight at 473 K under vacuum. X-ray photoelectron spectroscopy (XPS) was adopted to probe the near-surface compositions of the Na_2WO_4 promoted and unpromoted samples. The custom-built system consists of a vacuum chamber maintaining at a pressure of 1×10^{-9} Torr, a Thermo-Fisher Alpha 110 hemispherical energy analyzer, a Thermo-Fisher XR3, and a 300 W dual anode X-ray source, with an Al anode (1486.7 eV) was used for all analyses. For each sample, XPS narrow scans were taken for all metal cations (Ba 3d, Fe 2p, Al 2p, Na 1s, W 4f), C 1s, and O 1s. The CasaXPS program (Casa Software Ltd., U.K.) was used to analyze the XPS patterns, with the adventitious C 1s peak at 284.6 eV used for binding energy calibration.

Reactivity testing conditions

ROC tests with *n*-hexane were performed over a fixed bed of redox catalyst in a 1/8 in. ID quartz U-tube reactor which was positioned in a tube furnace and electrically heated. A K-type thermocouple and a temperature controller was used to control the temperature in the reaction zone. In each test, 0.5 g of redox

catalyst (250–850 μm diameter) was loaded into the quartz U-tube. To limit the gas volume in the heated zone, α-Al_2O_3 grit (16 mesh) was further added into the void space on both sides of the reactor. For comparison, blank tests with α-Al_2O_3 grit were also conducted at the same conditions. The gas flow rates and compositions in the reactor were controlled by mass flow controllers and an automated valve switching system.

To evaluate the activity of the redox catalyst for ROC of *n*-hexane, redox tests were conducted at various conditions. For the reduction step, 13 vol% of *n*-hexane vapor was introduced into the reactor by flowing Ar into a stainless-steel bubbler, which contained liquid *n*-hexane and was immersed in a water bath kept at 20 °C. For the oxidation step, 16.7 vol% of O_2 in Ar was used to regenerate the reduced catalyst material. Before and after each reduction step, a purge step with pure Ar was introduced to blow out any remaining gases. Prior *n*-hexane oxidative cracking test, the samples were subjected to 5 redox cycles comprising of 3 min reduction step with 80 vol% C_2H_6/Ar (in 60 mL min^{-1} Ar) and 3 min oxidation step with 16.7 vol% O_2/Ar (in 75 mL min^{-1} Ar) at 750 °C to stabilize the redox reactivity. During *n*-hexane redox test, 5 different temperature conditions (600–700 °C, with a step of 25 °C) and 3 different gas hourly space velocities (GHSV; 9000, 4500, 2250 h^{-1}) were investigated. For all conditions, the oxidation step and the purge step were 3 min and 5 min, respectively. During the reduction step, the same volume of *n*-hexane vapor (~7.5 mL, at 20 °C and 1 atm) was flowed into the reactor at different GHSV, by adjusting the injection time of *n*-hexane/Ar flow accordingly. Taking the 9000 h^{-1} GHSV condition as an example, 120 mL min^{-1} Ar was introduced into the bubbler to generate saturated *n*-hexane vapor and another 30 mL min^{-1} Ar was added before entering the U-tube reactor for a reaction duration of 20 s. For each test condition, 4 redox cycles were conducted and the effluent gas at the 3rd reduction step was collected for gas chromatography (GC). To investigate the long-term cyclic redox reactivity of the 20-NaW/BaFe6 sample, 30 redox cycles were performed at 2250 h^{-1} GHSV and 700 °C.

The gas products from ROC of *n*-hexane was analyzed by an Agilent 7890 Series Fast RGA GC. For the GC analysis, two thermal conductivity detector (TCD) channels were used for H_2 (Ar/TCD channel) and CO/CO_2 (He/TCD channel) identification, respectively, while a flame ionization detector (FID) channel was used for hydrocarbon separation. Calibration of the GC signals was conducted before measurement, using a refinery gas calibration standard. The concentration of different gas products was quantified by calculating the integral value of the signal peak. The *n*-hexane conversion and selectivity to different carbonaceous products were calculated *via* carbon balance. Water formation was calculated based on H atomic balance of all detected products. All cycles tested without GC measurement were analyzed by an MKS Cirrus II mass spectrometer for possible coke quantification as well as verifying GC results.

Results and discussion

Characterization of the as-prepared redox catalysts

Hexaaluminate phase can take the form of β-Al_2O_3 (JCPDS No. 1-75-707) and magnetoplumbite (MP) (JCPDS No. 1-84-1788) phases, depending on the radius and charge of large cations. Fig. 2 shows the XRD patterns of the five as-prepared $BaFe_xAl_{12-x}O_{19}$ (x = 1, 2, 3, 4, 6) samples. For x = 1 and 2, a well-crystallized β-Al_2O_3 hexaaluminate phase was attained. Compared with x = 1, the enlargement of cell parameters of the β-Al_2O_3 phase at x = 2 (Table 1) indicated that more Al ions ($r(Al^{3+})$ = 0.51 Å) in the β-Al_2O_3 lattice have been replaced by the larger Fe cations ($r(Fe^{3+})$ = 0.64 Å). When x increased from 2 to 3, in addition to the β-Al_2O_3 phase, diffraction peaks at 2θ = 31.3° and 35.1° were also clearly observed, which were associated with the MP-type hexaaluminate. The diffraction peaks corresponding to the MP phase became even stronger while the β-Al_2O_3 phase became weaker from x = 0 to x = 4, and eventually, no β-Al_2O_3 peaks were observed at x = 6. This result demonstrated that the increase of Fe ions introduction into the BHA structure facilitated the phase transformation from β-Al_2O_3 to MP, which was consistent with previous literature.[31] It should be noted that, at x = 6, besides the major diffraction peaks of MP phase, a small peak around 2θ = 28.2° was also observed which was associated with the $BaAl_2O_4$ spinel phase.

The BET surface areas of the $BaFe_xAl_{12-x}O_{19}$ samples are also summarized in Table 1. As can be seen, the surface area of the Fe-substituted BHAs generally shows a decreasing trend with the increase of Fe-substitution level. This can be explained by the inferior sintering-resistance of Fe cations than Al cations in the hexaaluminate structure. As such, higher Fe content would make the resulted material more prone to sintering at the high calcination temperature and hence smaller surface area.[31]

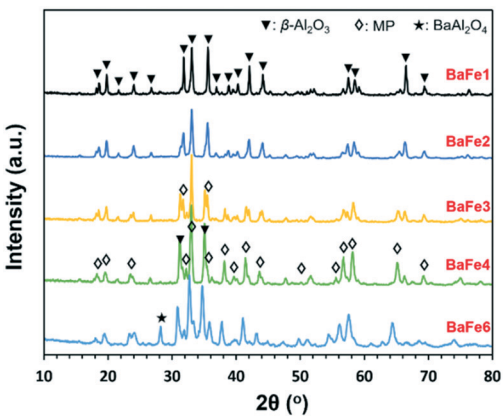

Fig. 2 XRD patterns for the fresh $BaFe_xAl_{12-x}O_{19}$ samples (x = 1, 2, 3, 4, 6). Notes: BaFe1 represents $BaFeAl_{11}O_{19}$, BaFe2 represents $BaFe_2Al_{10}O_{19}$, and so on; β-Al_2O_3 indicates β-Al_2O_3-type hexaaluminate phase; MP means magnetoplumbite-type hexaaluminate phase.

Table 1 BET surface areas and cell parameters for the five as-prepared $BaFe_xAl_{12-x}O_{19}$ samples (x = 1, 2, 3, 4, 6)

Samples	Surface area ($m^2\ g^{-1}$)	Pore volume ($cm^3\ g^{-1}$)	Pore size (nm)	Cell parameters (Å)			
				β-Al_2O_3		MP	
				$a_0 = b_0$	c_0	$a_0 = b_0$	c_0
$BaFe_1Al_{11}O_{19}$	15.6	0.0041	2.1	5.62	22.78	—	—
$BaFe_2Al_{10}O_{19}$	6.4	0.0015	2.1	5.62	22.78	—	—
$BaFe_3Al_9O_{19}$	8.2	0.0019	2.1	5.62	22.78	5.72	22.69
$BaFe_4Al_8O_{19}$	11.3	0.0028	2.1	5.63	22.78	5.74	22.72
$BaFe_6Al_6O_{19}$	11.3	0.0029	2.1	—	—	5.75	22.75

$BaFe_xAl_{12-x}O_{19}$ as redox catalysts in ROC of *n*-hexane

The activity of the as-prepared redox catalysts in ROC of *n*-hexane was first examined isothermally at 700 °C. Blank tests were also performed with α-Al_2O_3 grit-packed bed to determine the contribution of thermal cracking. All reaction characteristics, including *n*-hexane conversion and selectivity to light olefins and CO_x (CO/CO_2), are shown in Fig. 3. It can be seen that the presence of the redox catalysts can significantly enhance *n*-hexane conversion in comparison with thermal cracking (*e.g.*, 77.9% conversion for BaFe6, 35.9% for BaFe1 *vs.* 15.0% for blank at 700 °C and 9000 h^{-1}). Increasing Fe content in $BaFe_xAl_{12-x}O_{19}$ samples was found to be beneficial for attaining higher *n*-hexane conversion, which doubled when the Fe substitution increased from x = 1 to x = 6 (BaFe1 to BaFe6). This result is anticipated, since higher Fe content in the hexaaluminate structure leads to larger amount of active lattice oxygen.[27] Nevertheless, all the tested $BaFe_xAl_{12-x}O_{19}$ (x = 1, 2, 3, 4, 6) samples showed significant combustion activity towards hydrocarbons (*i.e.*, *n*-hexane and/or *n*-hexane cracking products), resulting in significant CO_x (mostly CO_2) selectivity and poor light olefin selectivity (*e.g.*, 70.8% CO_x selectivity *vs.* 20.2% olefin selectivity for BaFe6 at 700 °C and 9000 h^{-1}). The advantage of the high *n*-hexane conversions attained *via* the presence of redox catalysts was counteracted by the low olefin selectivity (*e.g.*, 15.7% olefins yield for BaFe6 *vs.* 12.8% olefin yield for thermal cracking at 700 °C and 9000 h^{-1}). Owing to their high CO_x selectivity, the as-prepared $BaFe_xAl_{12-x}O_{19}$ samples were not suitable for ROC of *n*-hexane to yield light olefins.

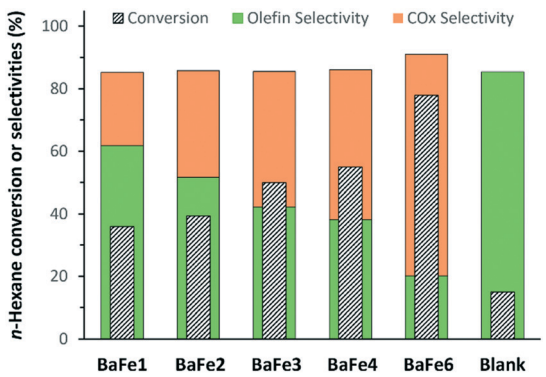

Fig. 3 Reaction characteristics of the five $BaFe_xAl_{12-x}O_{19}$ base samples (x = 1, 2, 3, 4, 6) in ROC of *n*-hexane. Reaction conditions: T = 700 °C; GHSV = 9000 h^{-1} (F_{Ar} = 150 mL min^{-1}, m = 0.5 g); *n*-hexane concentration in Ar, $C_{n\text{-hexane}} \approx$ 13 vol%; ROC reaction duration was 20 s within each cycle.

Effect of Na_2WO_4 promotion

In our previous studies for chemical looping oxidative dehydrogenation (CL-ODH) of ethane, it was found that promotion of the base redox catalysts with Na_2WO_4 was highly effective to suppress CO_x formation.[32–35] Moreover, the H_2 formed from ethane dehydrogenation can be selectively combusted by the Na_2WO_4-promoted redox catalysts, shifting the equilibrium of the ethane dehydrogenation reaction forward, thus enhancing the ethylene production. In view of these results, we adopted a similar Na_2WO_4 promotion strategy over the BaFe6 sample, expecting to increase the light olefins yield. BaFe6 was chosen for Na_2WO_4 promotion here due to its high activity for *n*-hexane conversion.

Fig. 4a shows the changes in products selectivity as well as *n*-hexane conversion of BaFe6 before and after promotion with different amounts of Na_2WO_4, *i.e.*, 5 wt% (5-NaW/BaFe6), 10 wt% (10-NaW/BaFe6), and 20 wt% (20-NaW/BaFe6), in ROC of *n*-hexane at 700 °C and 9000 h^{-1}. Results from thermal background under the same reaction condition are also provided for comparison purpose. As can be seen, when compared with the base BaFe6 sample, even with only 5 wt% of Na_2WO_4 promotion would contribute to notable selectivity changes in *n*-hexane oxidative cracking: the light olefins selectivity doubled, and CO_x selectivity decreased from 70.8% to 52.0%. With the increase of the Na_2WO_4 dopant amount from 5 wt% to 20 wt%, the promoted BaFe6 sample showed further decline in CO_x selectivity, and very low CO_x selectivity of 3.7% was achieved for the 20-NaW/BaFe6. Simultaneously, the light olefin selectivity increased significantly to as high as 83.9%, which was comparable to that of 85.2% attained in thermal cracking. Together with the greatly promoted light olefins selectivity, the $(C_4^= + C_3^=)/C_2^=$ ratio also showed an increasing trend with Na_2WO_4 promotion, and the $(C_4^= + C_3^=)/C_2^=$ ratio reached 1.25 for the 20-NaW/BaFe6. Meanwhile, the CH_4 selectivity attained for 20-NaW/BaFe6 sample was slightly lower than that of thermal cracking (7.8% *vs.* 10.5%). It is also noted that promotion of the base BaFe6 sample with Na_2WO_4 had an adverse effect on the activity of the redox catalyst: *n*-hexane conversion decreased substantially for all the promoted samples compared to their unpromoted counterparts. This may be partially attributed to the physical blocking of pores by Na_2WO_4 on the surface, as evidenced by the decreased BET surface area of the promoted samples (10.1 $m^2\ g^{-1}$, 7.8 $m^2\ g^{-1}$, and 7.3 $m^2\ g^{-1}$ for 5-NaW/BaFe6, 10-NaW/BaFe6, and 20-NaW/BaFe6, respectively). More detailed explanation on the reactivity change of the promoted samples will be given in the XPS analysis section. We note that the 31.0% *n*-hexane conversion attained for the 20-NaW/BaFe6 at 700 °C and 9000 h^{-1} was over twice as that as thermal cracking,

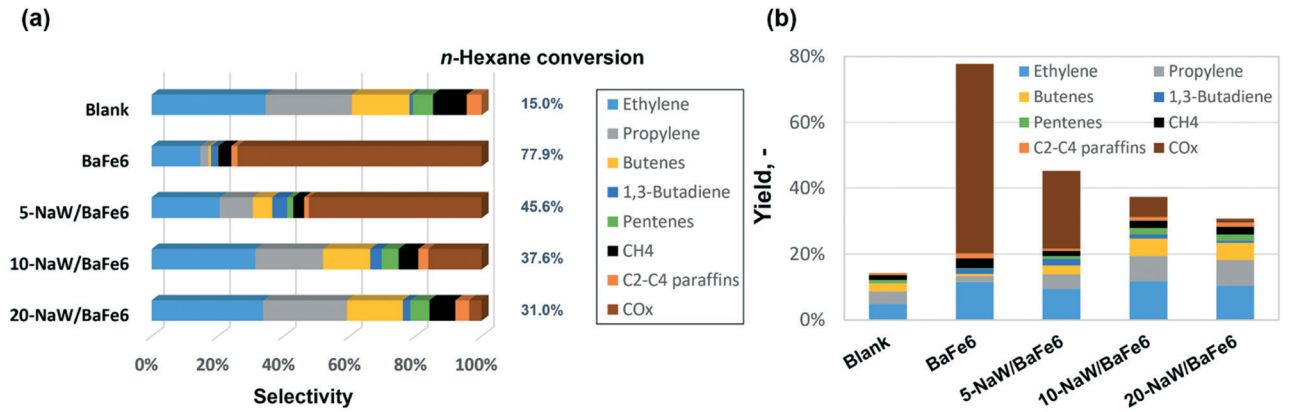

Fig. 4 (a) Changes in selectivity of $BaFe_6Al_6O_{19}$ after promotion with different amounts of Na_2WO_4 in *n*-hexane cracking. (b) Products yields of $BaFe_6Al_6O_{19}$ after promotion with different amounts of Na_2WO_4 in *n*-hexane cracking. Reaction condition: T = 700 °C; GHSV = 9000 h^{-1} (F_{Ar} = 150 mL min^{-1}, m = 0.5 g); *n*-hexane concentration in Ar, $C_{n\text{-hexane}} \approx$ 13 vol%. Blank corresponds to thermal cracking results.

which showed 15.0% *n*-hexane conversion. For more details on the selectivity data one can refer to Table S1 in ESI.†

Fig. 4b further illustrates the yields of different gas products in *n*-hexane cracking of the above tests. As can be seen, the olefin yield attained over α-Al_2O_3 grit (thermal cracking) was the smallest (12.8%) among all the tested samples. Conversely, the base BaFe6 sample was too reactive and most of the hydrocarbons were oxidized to undesired CO_x products (with a CO_x yield of 55.2%). At 700 °C, the olefin yield (15.7%) attained was only slightly higher in comparison with thermal cracking due to the significant decrease in olefin selectivity. 5 wt% Na_2WO_4 promotion onto the base BaFe6 sample led to the decrease of CO_x yield by over a half, while the light olefins yield increased to 19.5%. With the increase of Na_2WO_4 promotion amount to 10 wt%, an obvious decrease in CO_x yield was still observed (6.0% CO_x yield), and the highest olefin yield of 28.0% was attained among all the tested samples. Further promotion of BaFe6 with 20 wt% of Na_2WO_4 only slightly decreased the olefin yield to 26.0%, but the resulting CO_x yield turned to be significantly smaller (1.2%). Compared against the *n*-hexane thermal cracking results attained with α-Al_2O_3 grit, 20-NaW/BaFe6 exhibited an over doubled light olefin yield under the ROC (olefin yield of 12.8% in blank *vs.* 26.0% in ROC at 700 °C and 9000 h^{-1}), demonstrating the superiority of ROC of *n*-hexane with 20-NaW/BaFe6 as a redox catalyst over thermal cracking.

From the above results, it is clear that Na_2WO_4 promotion of the BaFe6 sample can alter its combustion characteristics towards *n*-hexane cracking products (hydrocarbons and H_2). To further understand such change of BaFe6 before and after Na_2WO_4 promotion, ROC of *n*-hexane tests with both BaFe6 base sample and 20-NaW/BaFe6 sample were conducted over the temperature range of 600–700 °C. Fig. 5 shows the selectivity towards CO_x and olefins for both samples at 9000 h^{-1} and different temperatures. As can be seen, the CO_x selectivity of the base BaFe6 sample was always higher than 70.8%, and the highest CO_x selectivity was attained as 80.5% at the lowest temperature condition. After being promoted by 20 wt% of Na_2WO_4, the CO_x selectivity of the 20-NaW/BaFe6 sample decreased by 10–20 times relative to the base BaFe6 sample over the investigated temperature range. Note that for both unpromoted and promoted BaFe6 samples, the H_2 formed was fully converted under all the tested conditions. The low CO_x selectivity achieved for the 20-NaW/BaFe6 sample can be attributed to its highly selective hydrogen combustion (SHC) property. To be more specific, 20 wt% Na_2WO_4 promotion of the base BaFe6 sample greatly suppressed the activation of hydrocarbons on the catalyst surface, while maintaining facile combustion of the generated H_2. Moreover, the CO_x selectivity for both unpromoted and promoted samples was more significant at lower temperatures, which can be explained by the different activation temperatures of non-selective and selective oxygen species: the non-selective oxygen (usually believed to be surface, electrophilic oxygen species) are relatively abundant at lower temperatures, while

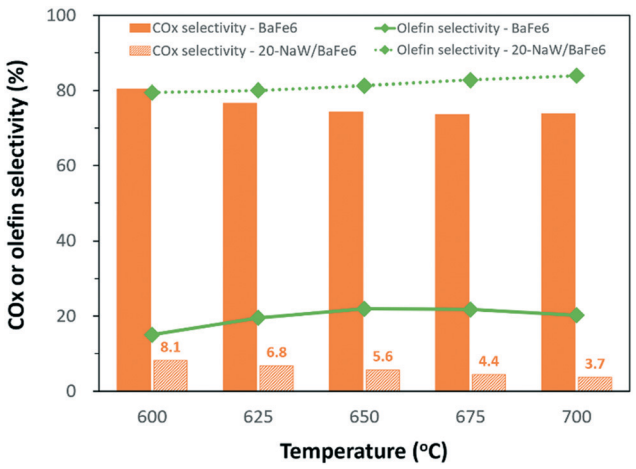

Fig. 5 Effect of 20 wt% Na_2WO_4 promotion over $BaFe_6Al_6O_{19}$ (20-NaW/BaFe6) on the CO_x and olefin selectivities within the temperature range of 600–700 °C. Reaction condition: GHSV = 9000 h^{-1} (F_{Ar} = 150 mL min^{-1}, m = 0.5 g); *n*-hexane concentration in Ar, $C_{n\text{-hexane}} \approx$ 13 vol%.

for the selective oxygen (lattice oxygen species), higher temperature is required to enable sufficient oxygen diffusion rate from bulk phase to the surface for the chemical looping reaction.[36,37] As also noted, despite the decreased CO_x selectivity with the increase of reaction temperature, the CO_x yield showed a continued increase from 0.6% (at 600 °C) to 1.2% (at 700 °C), resulting from the higher *n*-hexane conversion at elevated temperatures.

Effect of reaction temperature

Next, we compared the ROC of *n*-hexane over 20-NaW/BaFe6 to *n*-hexane thermal cracking (blank tests) within the temperature range of 600–700 °C. As shown in Fig. 6, the *n*-hexane conversion attained for thermal cracking was insignificant at the low temperature range (600–650 °C). With further increase of the reaction temperature, the *n*-hexane conversion achieved by thermal cracking at 700 °C was comparable with that achieved by ROC of *n*-hexane at 650 °C. Meanwhile, the olefin selectivity of the 20-NaW/BaFe6 was mostly preserved as compared to the thermal cracking (with minor losses due to CO_x formation from non-selective combustion). Consequently, significantly higher olefin yield was attained with the 20-NaW/BaFe6 than that from thermal cracking at the same reaction temperature. The superior olefin yield featured by the 20-NaW/BaFe6 over thermal cracking should not only be ascribed to the lattice oxygen donation of the redox catalyst, but also to the SHC capability resulting from Na_2WO_4 promotion. The CO_x yield was always lower than 1.2% in ROC of *n*-hexane at the tested conditions. Moreover, the H_2 generated was completely converted to H_2O *via* selective combustion by lattice oxygen, which led to the higher *n*-hexane conversion.

In order to obtain a more comprehensive understanding of the temperature effect on ROC of *n*-hexane, the distribution of *n*-hexane cracking products over the 20-NaW/BaFe6 was examined. Table 2 summarizes the key performance indices of the 20-NaW/BaFe6 in ROC of *n*-hexane at 9000 h^{-1} and three typical temperatures (600, 650, and 700 °C). For comparison, results from *n*-hexane thermal cracking at 600 °C and 700 °C are also provided. Note that in all these tests, no obvious coking or aromatic compounds were observed. Generally, higher temperatures were not beneficial to preserve longer-chain olefins due to the higher cracking severity, but the total selectivity to light olefins did show a slight increase with temperature for both ROC and thermal cracking processes. In both cases, the *n*-hexane conversion was significantly temperature-dependent, which increased from 0.5% to 15.0% for thermal cracking and 7.2% to 31.0% for ROC with a temperature change from 600 °C to 700 °C. CH_4 formation also slightly increased with the increase of reaction temperature, but lower CH_4 selectivity was attained by ROC in comparison with thermal cracking. For ROC of *n*-hexane, a critical property is the combustion characteristics of the redox catalyst towards *n*-hexane cracking products, which should be minimized. Using 20-NaW/BaFe6 as redox catalyst, the CO_x formation was effectively suppressed. Moreover, the CO_x selectivity showed an obvious decreasing trend with the increase of temperature, and the lowest CO_x selectivity of 3.7% was attained at 700 °C. Despite the suppressed lattice oxygen donation of the 20-NaW/BaFe6, complete H_2 combustion were achieved at all temperatures, indicating the superior SHC capability of this redox catalyst in ROC of *n*-hexane. From a process energy balance standpoint, complete combustion of H_2 formed would significantly decrease the endothermicity for naphtha conversion. This will lead to significant decrease in energy consumption and CO_2 emission.

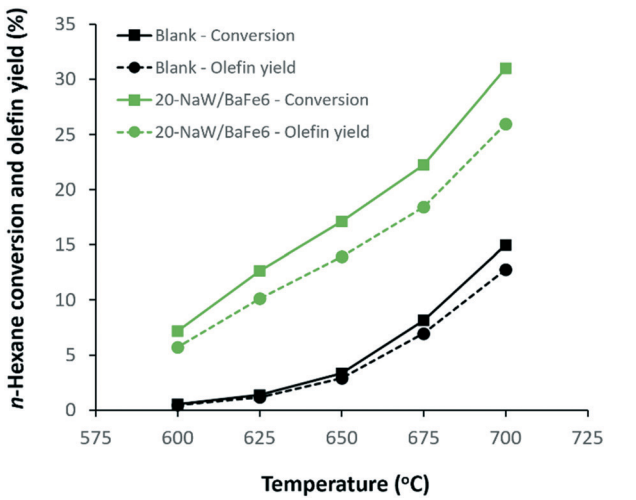

Fig. 6 *n*-Hexane conversion and olefin yield of 20-NaW/BaFe6 over a range of temperatures, with *n*-hexane thermal cracking over Al_2O_3 (blank) as comparison. Reaction condition: GHSV = 9000 h^{-1} (F_{Ar} = 150 mL min^{-1}, *m* = 0.5 g); *n*-hexane concentration in Ar, $C_{n\text{-hexane}} \approx 13$ vol%.

Effect of GHSV

The effect of space velocity on the performance of the 20-NaW/BaFe6 in ROC of *n*-hexane was also investigated. Fig. 7 shows the changes in *n*-hexane conversion and selectivity as

Table 2 Product distribution of ROC of *n*-hexane over 20-NaW/BaFe6 at various temperatures. Results of thermal cracking (blank) at 600 °C and 700 °C are shown for comparison. Reaction condition: GHSV = 9000 h^{-1} (F_{Ar} = 150 mL min^{-1}, *m* = 0.5 g); *n*-hexane concentration in Ar, $C_{n\text{-hexane}} \approx 13$ vol%

	600 °C (*Blank*)	600 °C	650 °C	700 °C	700 °C (*Blank*)
Conversion (mol%)					
n-Hexane	0.5	7.2	17.1	31.0	15.0
H_2 (to H_2O)	—	100.0	100.0	100.0	—
Selectivity (mol%)					
CO/CO_2	—	8.1	5.6	3.7	—
CH_4	10.1	6.7	7.3	7.8	10.5
C_2H_4	29.6	26.1	29.5	33.6	35.4
C_3H_6	28.6	26.5	25.9	25.2	26.0
Butenes	20.2	19.5	18.2	16.9	17.3
1,3-Butadiene	0	0.5	0.9	2.2	0.9
Pentenes	5.9	6.8	6.6	5.8	5.5
C_2-C_4 alkanes	5.1	5.3	5.2	4.2	4.3

the GHSV decreased from 9000 h^{-1} to 2250 h^{-1} at constant reaction temperature of 700 °C. As expected, a decrease in GHSV led to an increase in *n*-hexane conversion, together with only slightly decreased olefin selectivity. Consequently, the olefin yield increased from 26.0% at 9000 h^{-1} to 32.6% at 2250 h^{-1}. The CO_x selectivity and CH_4 selectivity did not experience a significant change with the decrease of GHSV. As also noted, complete H_2 conversion was attained at 9000 h^{-1}, but can only reach 88.5% and 81.1% at 4500 h^{-1} and 2250 h^{-1}, respectively. No coke was formed under the tested conditions, and complete data of reaction results at various GHSV are presented in Table S2 of ESI.†

Redox stability

Finally, the physicochemical stability of the 20-NaW/BaFe6 was evaluated *via* long-term redox cycling at 700 °C and 2250 h^{-1}. Fig. 8 presents the *n*-hexane conversion, olefin yield, and CO_x yield, as well as H_2 combustion, attained in ROC of *n*-hexane over 30 redox cycles. Stable olefin yield of 31.3–32.4% and low CO_x yield of 0.6–0.7% was attained during the 30 redox cycles. This indicates that the 20-NaW/BaFe6 was capable of withstanding the cyclic redox and thermal stress under the ROC scheme. As such, it could be a promising redox catalyst for ROC of naphtha.

XPS analysis of the redox catalysts

To elucidate the role of the (near) surface properties of the redox catalyst towards the activity and selectivity of BaFe6-based oxides for *n*-hexane ROC, we conducted XPS analysis on the as-prepared base BaFe6 and three additional samples with 5, 10, and 20 wt% Na_2WO_4 promotion; cycled versions of BaFe6 and 20-NaW/BaFe6 were also tested. Table 3 shows the near-surface atomic percentages of each of the four redox catalysts on a metal cation basis (*i.e.* excluding C and O), as well as the surface enrichment or suppression of each metal cation relative to its formula molar amount, given in parentheses. A value greater than 1 indicates an enriched metal cation, while suppression is denoted by a value less than 1.

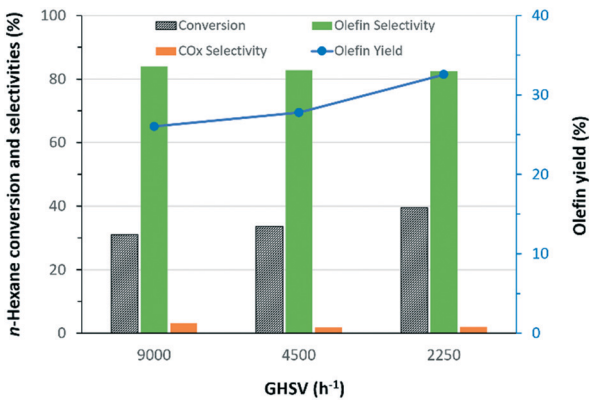

Fig. 7 Reaction characteristics of 20-NaW/BaFe6 in ROC of *n*-hexane at different GHSV. Reaction condition: T = 700 °C; *n*-hexane concentration in Ar, $C_{n\text{-hexane}} \approx$ 13 vol%; reaction duration was 20 s for 9000 h^{-1}, 40 s for 4500 h^{-1}, and 80 s for 2250 h^{-1} within each redox cycle.

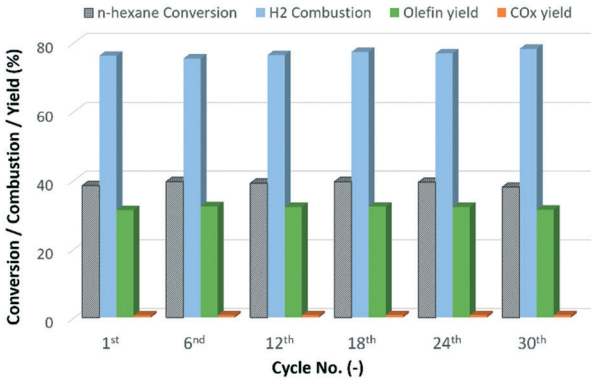

Fig. 8 Cyclic reactivity stability of 20-NaW/BaFe6 in ROC of *n*-hexane during 30 cycles. Reaction condition: T = 700 °C; GHSV = 2250 h^{-1} (F_{Ar} = 37.7 mL min^{-1}, m = 0.5 g); *n*-hexane concentration in Ar, $C_{n\text{-hexane}} \approx$ 13 vol%; reaction duration was 80 s within each redox cycle.

In each of the four as-prepared samples, Fe is significantly suppressed relative to its expected amount from stoichiometry, and Ba is present in slightly less than expected proportion, while Al is significantly enriched in the near-surface of each sample. Promotion of the base BaFe6 with Na_2WO_4 had the following effects: (i) the extent of Ba suppression increased with Na_2WO_4 loading, with 20-NaW/BaFe6 showing the least surface Ba and the greatest degree of suppression; (ii) Fe and Al surface percentages generally decreased with increasing Na_2WO_4, but only to the extent expected from the sample stoichiometry, *i.e.* the enrichment of Al and suppression of Fe were largely independent of Na_2WO_4 weight percentage; (iii) Na and W were enriched to the surface of the BaFe6 for all three loading levels, but the relative enrichment decreased going from 5 wt% to 20 wt% (in the case of W, from 4.83 to 1.38), indicating that Na_2WO_4 loading levels higher than 10 wt% may not further increase the near surface concentrations of Na and W.

Further differences between the base BaFe6 and the 20-NaW/BaFe6 sample appeared upon redox cycling. Whereas near-surface Ba was suppressed for the fresh BaFe6, cycling of the material led to a barium enrichment (from 0.73 to 1.17 compared to bulk stoichiometry). Meanwhile, near surface Fe was further suppressed after the redox cycles (from 0.40 to 0.24). In contrast, the Ba content of cycled 20-NaW/BaFe6 was identical to that of the fresh 20-NaW/BaFe6, indicating that the Na_2WO_4 promoter inhibited the migration/enrichment of Ba to the near-surface region during redox cycling. While Na and W enrichment decreased slightly after redox cycling, both elements were retained on the surface of 20-NaW/BaFe6 in near-stochiometric proportion, indicating the stability of the Na_2WO_4-promoted BaFe6 against redox stresses. Taken together with the reaction testing results for BaFe6 and 20-NaW/BaFe6, the increase in olefin selectivity observed upon Na_2WO_4 promotion was likely related to the suppression of near-surface Ba during cycling, a product of the stable presence of Na_2WO_4 on the surface of the redox catalyst.

Table 3 Near-surface cation atomic percentages and relative surface enrichment/suppression for four as-prepared redox catalysts (BaFe6, 5-NaW/BaFe6, 10-NaW/BaFe6, and 20-NaW/BaFe6) and two cycled redox catalysts (BaFe6, 20-NaW/BaFe6), from XPS analysis

	Surface atomic percentage (relative enrichment/suppression)				
Sample	Ba 3d	Fe 2p	Al 2p	Na 1s	W 4f
BaFe6 (*fresh*)	5.6% (0.73)	17.8% (0.38)	76.6% (1.66)	—	—
5-NaW/BaFe6 (*fresh*)	4.6% (0.61)	17.2% (0.39)	64.2% (1.45)	8.0% (3.21)	6.0% (4.83)
10-NaW/BaFe6 (*fresh*)	4.6% (0.64)	16.9% (0.40)	59.3% (1.39)	11.8% (2.34)	7.5% (2.95)
20-NaW/BaFe6 (*fresh*)	3.7% (0.57)	15.0% (0.38)	62.8% (1.61)	11.4% (1.10)	7.2% (1.38)
BaFe6 (*cycled*)	9.0% (1.17)	10.9% (0.24)	80.1% (1.74)	—	—
20-NaW/BaFe6 (*cycled*)	3.7% (0.57)	10.5% (0.27)	70.8% (1.82)	9.5% (0.92)	5.5% (1.06)

Recent studies have indicated that the presence of surface alkali earth cations such as Sr^{2+} led to increased methane combustion under both co-feed[38] and redox conditions.[39]

Conclusions

The current work investigated the capability of Fe-substituted barium hexaaluminates ($BaFe_xAl_{12-x}O_{19}$) as redox catalyst for redox oxidative cracking (ROC) of naphtha (using *n*-hexane as the model compound) under a chemical looping scheme. Different Fe substitution levels were adopted to synthesize the $BaFe_xAl_{12-x}O_{19}$ (x = 1, 2, 3, 4, 6) samples. XRD characterization indicated the formation of pure hexaaluminate phases for most of the as-prepared samples, except for $BaFe_6Al_6O_{19}$ (BaFe6), in which minor $BaAl_2O_4$ spinel phase was observed. A higher level of Fe substitution was beneficial to attain higher oxygen carrying capacity, leading to more active redox catalysts towards *n*-hexane conversion. However, all the $BaFe_xAl_{12-x}O_{19}$ (x = 1, 2, 3, 4, 6) base samples showed high CO_x selectivity (23.4–70.8% at 700 °C and 9000 h^{-1}) in ROC of *n*-hexane.

20 wt% of sodium tungstate (Na_2WO_4) promotion onto the BaFe6 base sample (20-NaW/BaFe6) was found to be very effective to suppress CO_x formation (decreased to 3.7%) while retaining complete conversion of the generated H_2 at 700 °C and 9000 h^{-1}. This was mainly attributed to the high selective hydrogen combustion (SHC) property of 20-NaW/BaFe6. When compared with *n*-hexane thermal cracking, ROC of *n*-hexane with 20-NaW/BaFe6 as a redox catalyst showed a significant increase in olefin yield (0.5–12.8% in blank *vs.* 5.7–26.0% in ROC) at the temperature range of 600–700 °C and 9000 h^{-1}. Stable olefin yield (31.3–32.4%) and low CO_x yield (<0.7%) during 30 redox cycles at 700 °C and 2250 h^{-1} demonstrated the long-term stability of the 20-NaW/BaFe6. XPS analysis of cycled BaFe6 and 20-NaW/BaFe6 indicated that the Na_2WO_4 promoter inhibited the movement of Ba to the near-surface region during redox cycling, suggesting that Ba near-surface enrichment played a role in the CO_x selectivity of unpromoted samples. No major changes in Na and W near-surface enrichment occurred upon redox cycling, confirming the stability of the promoted redox catalyst during *n*-hexane ROC.

Conflicts of interest

There are no conflicts to declare.

Acknowledgements

This work was supported by the U.S. National Science Foundation (Award No. CBET-1604605), the US Department of Energy (RAPID Subaward DE-EE0007888-05-6), and the Kenan Institute for Engineering, Technology and Science at NC State University. The authors acknowledge the use of the Analytical Instrumentation Facility (AIF) at North Carolina State University, which is supported by the State of North Carolina and the National Science Foundation. Dr. Kun Zhao at Guangzhou Institute of Energy Conversion, Chinese Academy of Sciences, is acknowledged for her assistance on XPS measurements. The author X. Tian also acknowledges the financial support from the China Scholarship Council (CSC).

Notes and references

1 H. Zimmermann and R. Walzl, *Ullmann's Encycl. Ind. Chem.*, 2012, pp. 547–572, DOI: 10.1002/14356007.a10.
2 J. J. Sattler, J. Ruiz-Martinez, E. Santillan-Jimenez and B. M. Weckhuysen, *Chem. Rev.*, 2014, **114**, 10613–10653, DOI: 10.1021/cr5002436.
3 M. D. Porosoff, M. N. Z. Myint, S. Kattel, Z. Xie, E. Gomez, P. Liu and J. G. Chen, *Angew. Chem., Int. Ed.*, 2015, **54**, 15501–15505, DOI: 10.1002/anie.201508128.
4 B. Yan, S. Yao, S. Kattel, Q. Wu, Z. Xie, E. Gomez, P. Liu, D. Su and J. G. Chen, *Proc. Natl. Acad. Sci. U. S. A.*, 2018, 201806950, DOI: 10.1073/pnas.1806950115.
5 S. Lewandowski, Ethylene – Golobal, in: *Asia Chem. Conf.*, 2016, https://cdn.ihs.com/www/pdf/Steve-Lewandowski-Big-Changes-Ahead-for-Ethylene-Implications-for-Asia.pdf.
6 S. Sadrameli, *Fuel*, 2016, **173**, 285–297, DOI: 10.1016/j.fuel.2016.01.047.
7 T. Ren, M. Patel and K. Blok, *Energy*, 2006, **31**, 425–451, DOI: 10.1016/j.energy.2005.04.001.
8 I. Amghizar, L. A. Vandewalle, K. M. Van Geem and G. B. Marin, *Engineering*, 2017, **3**, 171–178, DOI: 10.1016/J.ENG.2017.02.006.
9 M. M. Bhasin, *Top. Catal.*, 2003, **23**, 145–149.
10 H. Krannila, W. O. Haag and B. C. Gates, *J. Catal.*, 1992, **135**, 115–124.
11 S. M. Babitz, B. A. Williams, J. T. Miller, R. Q. Snurr, W. O. Haag and H. H. Kung, *Appl. Catal., A*, 1999, **179**, 71–86.

12 S. Kotrel, M. P. Rosynek and J. H. Lunsford, *J. Catal.*, 1999, **182**, 278–281.
13 N. Katada, Y. Kageyama, K. Takahara, T. Kanai, H. Ara Begum and M. Niwa, *J. Mol. Catal. A: Chem.*, 2004, **211**, 119–130, DOI: 10.1016/j.molcata.2003.10.001.
14 H. Abrevaya, S. F. Abdo and R. L. Patton, *US Pat.*, 6867341, 2005.
15 N. Rahimi and R. Karimzadeh, *Appl. Catal., A*, 2011, **398**, 1–17, DOI: 10.1016/j.apcata.2011.03.009.
16 S. M. Alipour, *Chin. J. Catal.*, 2016, **37**, 671–680, DOI: 10.1016/S1872.
17 C. Boyadjian and L. Lefferts, *Eur. J. Inorg. Chem.*, 2018, **2018**, 1956–1968, DOI: 10.1002/ejic.201701280.
18 X. Liu, W. Li, H. Xu and Y. Chen, *React. Kinet. Catal. Lett.*, 2004, **81**, 203–209, DOI: 10.1023/B:REAC.0000019424.06619.28.
19 X. Liu, W. Li, H. Zhu, Q. Ge, Y. Chen and H. Xu, *Catal. Lett.*, 2004, **94**, 31–36, DOI: 10.1023/B:CATL.0000019327.86674.98.
20 C. Boyadjian, L. Lefferts and K. Seshan, *Appl. Catal., A*, 2010, **372**, 167–174, DOI: 10.1016/j.apcata.2009.10.030.
21 V. P. Haribal, Y. Chen, L. Neal and F. Li, *Engineering*, 2018, **4**, 714–721, DOI: 10.1016/j.eng.2018.08.001.
22 A. H. Elbadawi, M. Y. Khan, M. R. Quddus, S. A. Razzak and M. M. Hossain, *AIChE J.*, 2017, **63**, 130–138, DOI: 10.1002/aic.
23 J. Adanez, A. Abad, F. Garcia-Labiano, P. Gayan and L. F. de Diego, *Prog. Energy Combust. Sci.*, 2012, **38**, 215–282, DOI: 10.1016/j.pecs.2011.09.001.
24 M. Bellotto, G. Artioli, C. Cristiani, P. Forzatti and G. Groppi, *J. Catal.*, 1998, **179**, 597–605.
25 A. J. Zarur and J. Y. Ying, *Nature*, 2000, **403**, 65.
26 M. Tian, X. Wang and T. Zhang, *Catal. Sci. Technol.*, 2016, **6**, 1984–2004, DOI: 10.1039/c5cy02077h.
27 M. Tian, X. Wang, X. Liu, A. Wang and T. Zhang, *AIChE J.*, 2016, **62**, 792–801, DOI: 10.1002/aic.
28 Y. Zhu, W. Liu, X. Sun, X. Ma, Y. Kang, X. Wang and J. Wang, *AIChE J.*, 2018, **64**, 550–563, DOI: 10.1002/aic.15942.
29 G. Groppi, C. Cristiani and P. Forzatti, *J. Catal.*, 1997, **168**, 95–103.
30 G. Groppi, M. Bellotto, C. Cristiam, P. Forzatti and P. Villa, *Appl. Catal., A*, 1993, **104**, 101–108.
31 Y. Zhu, X. Wang, G. Wu, Y. Huang, Y. Zhang, J. Wang and T. Zhang, *J. Phys. Chem. C*, 2011, **116**, 671–680, DOI: 10.1021/jp2067414.
32 L. M. Neal, S. Yusuf, J. A. Sofranko and F. Li, *Energy Technol.*, 2016, **4**, 1200–1208, DOI: 10.1002/ente.201600074.
33 S. Yusuf, L. M. Neal and F. Li, *ACS Catal.*, 2017, **7**, 5163–5173, DOI: 10.1021/acscatal.7b02004.
34 R. B. Dudek, Y. Gao, J. Zhang and F. Li, *AIChE J.*, 2018, **64**, 3141–3150, DOI: 10.1002/aic.16173.
35 S. Yusuf, L. Neal, V. Haribal, M. Baldwin, H. H. Lamb and F. Li, *Appl. Catal., B*, 2018, **232**, 77–85, DOI: 10.1016/j.apcatb.2018.03.037.
36 A. Shafiefarhood, J. C. Hamill, L. M. Neal and F. Li, *Phys. Chem. Chem. Phys.*, 2015, **17**, 31297–31307, DOI: 10.1039/c5cp05583k.
37 A. Shafiefarhood, J. Zhang, L. M. Neal and F. Li, *J. Mater. Chem. A*, 2017, **5**, 11930–11939, DOI: 10.1039/C7TA01398A.
38 F. Polo-Garzon, V. Fung, X. Liu, Z. D. Hood, E. E. Bickel, L. Bai, H. Tian, G. S. Foo, M. Chi, D.-e. Jiang and Z. Wu, *ACS Catal.*, 2018, **8**, 10306–10315, DOI: 10.1021/acscatal.8b02307.
39 R. B. Dudek, X. Tian, M. Blivin, L. M. Neal, H. Zhao and F. Li, *Appl. Catal., B*, 2019, **246**, 30–40, DOI: 10.1016/j.apcatb.2019.01.048.

